Defence Technology 17 (2021) 715–727

Contents lists available at ScienceDirect

Defence Technology

journal homepage: www.keaipublishing.com/en/journals/defence-technology

Effect of friction stir processing on mechanical properties and heat transfer of TIG welded joint of AA6061 and AA7075

Husain Mehdi*, R.S. Mishra

Department of Mechanical Engineering, Delhi Technological University, Delhi, India

ARTICLE INFO

Article history:
Received 7 January 2020
Received in revised form
4 March 2020
Accepted 22 April 2020
Available online 7 May 2020

Keywords:
Residual stress
TIG+FSW
Heat transfer
Micro-hardness
Tensile strength

ABSTRACT

Tungsten inert gas (TIG) welding is the most commonly used joining process for aluminum alloy for AA6061 and AA7075 which are highly demanded in the aerospace engineering and the automobile sector, but there are some defects occur during TIG welding like micro-crack, coarse grain structure, and porosity. To improve these defects, the TIG welded joint is processed using friction stir processing (FSP).

This paper presents the effect of friction stir processing on TIG welding with filler ER4043 and ER 5356 for dissimilar aluminum alloy AA6061 and AA7075. The mechanical characterization, finite element formulation and mathematical equations of heat transfer of TIG + FSP welded joints are investigated using ANSYS Fluent software by adjusting process parameters of FSP. The results show that the maximum compressive residual stress 73 MPa was obtained at the fusion zone (FZ) of the TIG weldment with filler ER4043, whereas minimum compressive residual stress 37 MPa was obtained at stir zone (SZ) of the TIG + FSP with filler 5356. The maximum heat flux 5.33 × 106 W/m2 and temperature 515 °C have observed at tool rotation 1600 rpm with a feed rate of 63 mm/min. These results give a satisfactory measure of confidence in the fidelity of the simulation

1. Introduction

Friction stir welding (FSW) is a solid-state joining process that uses a non-consumable tool to join similar or dissimilar materials. The FSW does not involve the melting of parent material, which have many advantages on conventional fusion welding processes [1]. The FSW process involves the heat generation, which produced by pressure and friction between the tool and the workpiece. As a result of the generated heat, the weldment surfaces in contact soften become plasticized [2]. The modern development in the automobile sector and defense sector have been transformed from conventional materials to light material such as aluminum alloy. Due to excellent physical and mechanical properties of Al-alloy such as high corrosion resistance, low density, high strength to weight ratio and high thermal conductivity, it is mostly used for making various components such as military aircraft, rocket, and rocket launcher, axle shafts, rims, bumpers, and car bodies. FSW is used in the fabrication of automotive and shipbuilding components, aircraft structural components and reducing structural weight [3–7]. To study material flow and temperature distribution in friction stir welding of similar or dissimilar aluminum alloys many authors developed the CFD model to analyze the plastic flow, heat transfer and heat generation in the welding process [8–10], and the effect of tool profile on the material flow [11–13]. Due to low heat generation in the friction stir welding, the residual stresses are also low in the weldment. The transverse force of friction stir welding tools plays an important role in stress measurement [14–16]. The residual stresses in the weldment have a big impact on the performance of the welded structure. So far, information on the residual stress distribution of FSW has been limited [17]. The effects of tool feed rate on residual stresses of FSW of Al-alloy joints were studied with synchrotron X-ray measurement and analyze the residual stresses in longitudinal and transverse directions [16]. Many researchers have used finite element methods for the residual stress distribution in FSW. The computational fluid dynamic supports the heat transfer model and heat source of friction stir welding. The residual stress depends on the empathetic of heat transfer during FSW, although the correct prediction of temperature distribution depends on the heat source [18–20]. FSW can affect the performance of the residual stresses in

* Corresponding author.
E-mail address: husainmehdi4u@gmail.com (H. Mehdi).
Peer review under responsibility of China Ordnance Society

https://doi.org/10.1016/j.dt.2020.04.014

Nomenclature

u	Plastic flow velocity	τ	Max. Shear stress
μ	Non-Newtonian viscosity	η	Mechanical efficiency
p	Pressure	ω	Angular velocity
ρ	Density	P_N	Normal pressure
U_1	Welding velocity	q_1	Total heat generation rate
z	Zener Hollomon parameter	T_a	Ambient temperature
a and n	Material constant	σ	5.67×10^{-16} J/(K^4 m^2 s)
Q	Temperature activation energy	ε	Convection heat transfer coefficient
Z	Temperature effective strain rate	h_b	Heat transfer coefficient
K	Thermal conductivity	σ_2	Friction stress
C_p	Specific heat	σ_1	Tensile stress
S_i	Heat generation rate	d	Main grain diameter
h_t	Emissivity at top surface	k	Constant
r	Radial distance from tool axis	R_S	Shoulder radius
A_r	Small area on tool pin	R_P	Tool pin radius
V	Control volume under A_r	h_{b0}	Heat transfer parameter of bottom.surface
θ	Angle of negative x-axis	μ_f	Spatially variable fraction slip.between the work piece and tool
		S_b	Heat generation rate due to plastic.deformation

the weldment and the processing parameters such as rotating tool may affect the development of residual stresses [21,22]. The mechanical properties, grain size are dependent on tool geometry, processing parameters and chemical composition of alloying elements. A new grain structure could be formed in friction stir welding by controlling the process parameter and heat input [23–27]. Comparison of residual stresses of TIG and FSW has been done for AA6061 and AA7075, and found that the longitudinal residual stress is larger than the traverse residual stress in the welded joint [28]. There are no successful investigations have been done to find out residual stress and heat transfer in TIG welded joint with friction stir processing. The small plate having the dimension of 150 mm × 25 mm × 0.8 mm, have been investigated, as a result, the properties at the beginning and end of the welded joints can be significantly different. The tensile strength first increases and then decreases with the growth of rotational speed. Three layers i.e. top, middle, and bottom, have considered measuring the microhardness of the welded joint. The top layer of the weld has a higher recrystallization degree and dynamic recovery and the bottom layer is strongly stirred under mechanical action of the tool pin such that each layer of welded joint shows the different mechanical properties [29]. A new welding approach of TIG+FSP was successfully applied to the AA2024 to enhance the mechanical properties of the TIG welded joints. They conclude that the defects and porosities in the TIG welded joints are completely reduced by the FSP process and modified the microstructure and mechanical properties of the TIG+FSP welded joint [30]. The application of FSP on the TIG welded joint improved the ductility and tensile strength of the FSW and TIG welded joint of AA5083-H111 and results revealed best-reduced dimple size [31].

In this work, the effect of FSP on TIG welding for dissimilar Al-alloy AA6061 and AA7075 with filler wire ER4043 and ER5356 was carried out and analyze the mechanical properties, residual stress distribution and heat transfer in (TIG+FSP) welded joint. The present study was focus on the improvement of mechanical properties and the residual stress distribution of the TIG-welded joint with different filler wire (ER4043 and ER5356) by using a friction stir processing approach. This topic is carefully selected after noticing that there is little literature review available on the TIG+FSP welding approach. The outcomes of this paper will give the new approach for enhancing the mechanical properties and heat transfer of TIG+FSP welded joints which play a huge role in welded structures.

2. Materials and methods

Two AA6061 and AA7075 aluminum alloy plates having dimensions (150 mm × 40 mm × 6.2 mm) were welded together using the TIG+FSP welding approach. V butt joints of 45° were prepared for TIG welding with the help of milling cutter and power hacksaw. There are two types of samples were prepared for TIG welded joint. In the first sample, ER4043 filler wire was used and for the second sample, ER 5356 filler wire was used. The chemical composition of filler rod and base materials are shown in Table 1. The processing parameters and filler wire are strappingly affected by the mechanical properties of the welded joint. In this work, the filler wire of ER4043 and ER5356 of diameter 2.4 mm were used to join a single V groove plate at voltage 22 V and current 50 amp for all welding processes. Argon (25 L/min) is used as a shielding gas and travel speed 3.6 mm/s to fabricate the joint.

After TIG welding, the FSP technique was used on TIG weldment to improve the welding quality and mechanical properties. The non-consumable H13 steel tool with pin diameter, shoulder diameter and a pin length of 3 mm, 19.5 mm, and 5.5 mm respectively was used. 0° tilt angle was used during friction stir processing on the AA6061 and AA7075 plate at a rotational speed of 800 rpm–1600 rpm and a traverse speed of 63 mm/min is shown in Fig. 1(a). The tool nomenclature is shown in Fig. 1(b). The processing parameters of TIG welding and friction stir processing are shown in Table 2 and Table 3.

Fig. 2 demonstrate the dimension of the tensile sub test specimen as per ASTM E8. The tensile test specimens were sliced and machined from the welded joint using a milling cutter and shaper machine. Single-pass FSP is used to fabricate TIG+FSP welded joint. Three sub tensile specimens were tested on a UTM machine at

Table 1
Chemical composition of filler wire and parent material.

Material	Si	Cu	Fe	Zn	Mg	Mn	Cr	Ti	Al
ER 4043	5.300	0.025	0.80	0.10	0.05	–	–	0.02	Bal.
ER 5356	0.025	0.015	0.15	0.01	4.90	0.14	0.11	0.09	Bal.
AA7075	0.580	1.200	0.35	5.10	2.10	0.12	0.20	0.05	Bal.
AA6061	0.400–0.800	0.200	0.70	0.25	0.80	0.10	0.20	0.15	Bal.

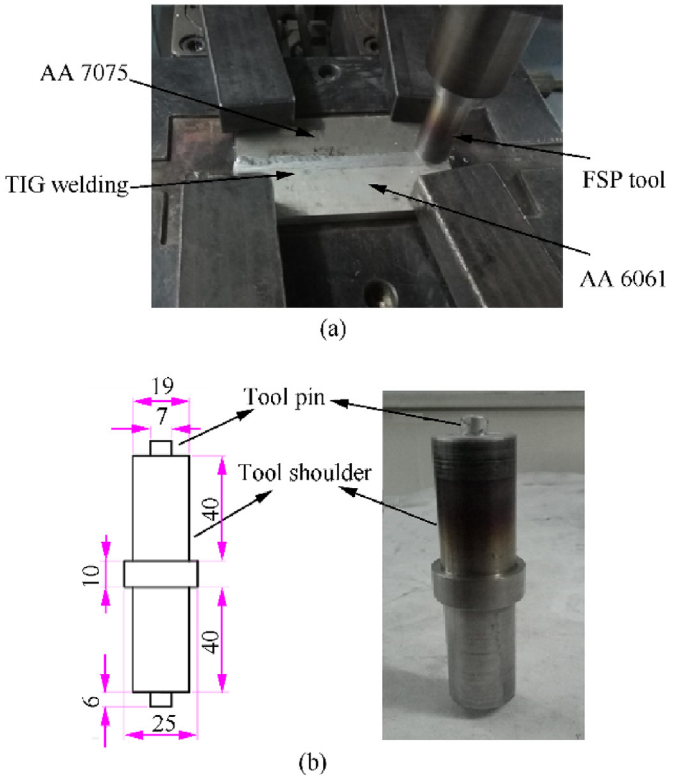

Fig. 1. (a) FSP process after TIG welding, (b) Friction stir processing tool of H13 tool steel.

room temperature and the average of these three results is taken. Vicker microhardness machine was used for measuring the hardness across the welded joints with a load of 100 g and dwell time 30 s. Microstructure observations were carried out using a scanning electron microscope (SEM) for TIG and TIG+FSP welded joints.

3. Numerical modeling [10]

For incompressible flow, the continuity equation in the direction of x, y and z is given by

$$\frac{\partial u_i}{\partial x_i} = 0 \tag{1}$$

The momentum conservation equation of the heat source is given as

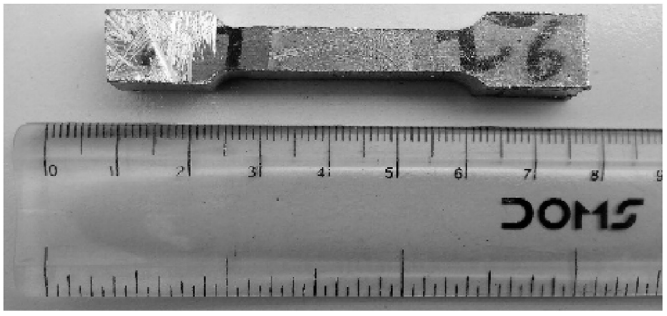

Fig. 2. Dimension of tensile test specimen as per ASTM E8.

$$\rho \frac{\partial u_I\, u_j}{\partial x_i} = -\frac{\partial P}{\partial x_j} + \frac{\partial}{\partial x_I}\left(\mu \frac{\partial U_j}{\partial x_i} + \mu \frac{\partial U_i}{\partial x_j}\right) - \rho\, U_1 \left(\frac{\partial U_j}{\partial x_I}\right) \tag{2}$$

The flow stress can be calculated as

$$\sigma_e = \frac{1}{\alpha} \sinh^{-1}\left[\left(\frac{z}{A}\right)^{1/n}\right] \tag{3}$$

$$A = 1.80 \times 106 + 1.74 \times 10^8 (\%C) - 6.5 \times 10^7 (\%C)^2 \tag{4}$$

$$\alpha = 1.07 + 1.70 \times 10^{-4} T - 2.8 \times 10^{-7} T^2 \tag{5}$$

$$n = 0.2 + 3.96 \times 10^{-4} T \tag{6}$$

$$z = \varepsilon \exp\left(\frac{Q}{RT}\right) \tag{7}$$

The effective strain may be written as

$$\varepsilon = \left(\frac{2}{3}\, \varepsilon_{ij} \varepsilon_{ij}\right)^{1/2} \tag{8}$$

Where ε_{ij} is given by

$$\varepsilon_{ij} = \frac{1}{2}\left(\frac{\partial u_i}{\partial x_j} + \frac{\partial u_j}{\partial x_i}\right) \tag{9}$$

So, the viscosity can be calculated as

$$\mu = \frac{\sigma_e}{3\varepsilon} \tag{10}$$

The thermal energy conservation equation at steady state is given by

Table 2
Processing parameters of TIG welded joint [32].

Working Parameters	Shielding Gas/(L·min^{-1})	Current/A	Electrode Diameter/mm	Voltage/V	Welding Speed/(mm·s^{-1})
Description	25 (Argon)	50	3.2	22	3.6

Table 3
Processing parameters of friction stir processing [33].

Sample No	Current	Welding Speed/(mm·min^{-1})	Tool rotational speed/rpm	Frequency	Tilt angle/(°)
1	6.9	63	800	28.52	0
2			1000	33.36	
3			1250	40.00	
4			1600	52.61	

$$\rho C_P \frac{\partial (u_i T)}{\partial x_i} = -\rho C_P U_1 \frac{\partial T}{\partial x_i} + \frac{\partial}{\partial x_i}\left(k \frac{\partial T}{\partial x_i}\right) + S_i + S_b \tag{11}$$

Then S_i may be written as

$$S_i = \left[(1-\delta)\eta\tau + \delta\mu_f P_N\right]\ (\omega_r - U_1 \sin\theta)\ \frac{A_r}{V} \tag{12}$$

During friction stir welding, mixing is not atomic, only grains structure is deformed not mixing of atoms.

$$\phi = 2\left[\left(\frac{\partial u_1}{\partial x_1}\right)^2 + \left(\frac{\partial u_2}{\partial x_2}\right)^2 + \left(\frac{\partial u_3}{\partial x_3}\right)^2\right] + \left(\frac{\partial u_1}{\partial x_2} + \frac{\partial u_2}{\partial x_1}\right)^2 + \left(\frac{\partial u_1}{\partial x_3} + \frac{\partial u_3}{\partial x_1}\right)^2 + \left(\frac{\partial u_3}{\partial x_2} + \frac{\partial u_2}{\partial x_3}\right)^2 \tag{13}$$

3.1. Boundary conditions

When the work-piece top surface away from the tool shoulder edge, the boundary condition for heat exchange involves both convection and radiation heat transfer. However, at the sides and the bottom surface of the work-piece, the boundary condition for heat exchange involves only convection heat transfer. The heat generation rate at the interface between tool and the work-piece can be given be given by

$$f = \frac{J_w}{J_T} = \frac{\sqrt{(k_\rho C_P)_W}}{\sqrt{(k_\rho C_P)_T}} \tag{14}$$

Where T and W denote the tool and work piece respectively. The heat flux continuity on the shoulder interface yields

$$k \frac{\partial T}{\partial z}\bigg|_{top} = \frac{J_w}{J_w + J_T}\ q1 \quad R_P \le r \le R_s \tag{15}$$

Where J_w and J_T are the heat conducted to the work-piece and tool respectively

$$J = \sqrt{k\rho\ C_p} \tag{16}$$

Where C_p is heat capacity, ρ and K are density and thermal conductivity respectively.

The total heat generation rate may be written as

$$q_1 = [\eta(1-\delta)\tau + \delta\mu f.P_H]\ (\omega r - U_1 \sin\theta) \tag{17}$$

The heat transfer coefficient may be calculated as.

$$k \frac{\partial T}{\partial z}\bigg|_{bottom} = h_b (T - T_a) \tag{18}$$

Value of h_b can be calculated as

$$h_b = h_{b0}(T - T_a)^{0.25} \tag{19}$$

The heat transfer due to radiation and convection is written as

$$k \frac{\partial T}{\partial z}\bigg|_{top} = h_t (T - T_a) + \sigma\varepsilon^1 \left(T^4 - T_a^4\right) \tag{20}$$

In this model, the computational region is considered as a single-phase visco-plastic non-Newtonian fluid and the FSW tool is considered as rotating in a fixed position as shown in Fig. 3. The material flows into the computational domain from the inlet velocity and out from outlet velocity at the welding speed (traverse speed). Top, bottom and side surfaces of the work-pieces are considered equivalent to the wall surface, having the same velocity as welding speed but opposite in direction.

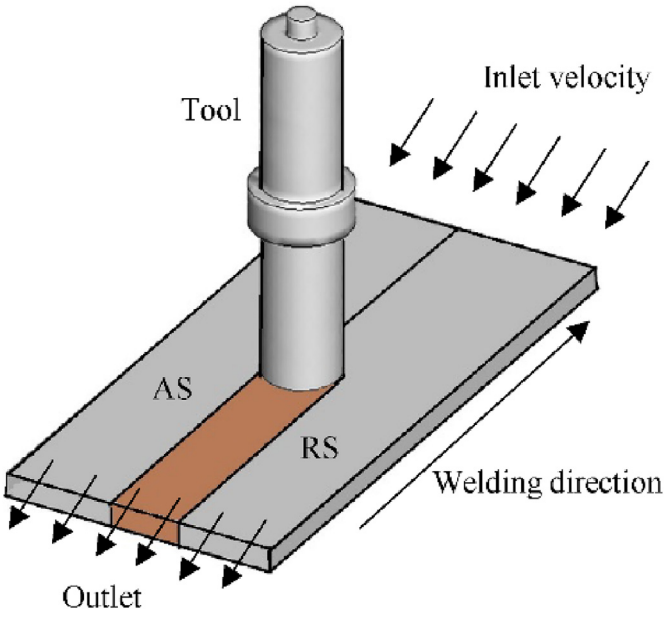

Fig. 3. Boundary condition.

Velocity at the tool pin periphery have been defined in terms of tool translation velocity and the tool pin angular velocity

$$\left.\begin{aligned} u &= (1-\delta)(\omega R_P \sin\theta - U_1) \\ v &= (1-\delta)\omega R_P \cos\theta \\ w &= k\frac{\omega}{2\pi} R_P \end{aligned}\right\},\ R_P \le r \le R_S \tag{21}$$

Similarly, at the shoulder contact, the velocity boundary condition may be written as

$$\left.\begin{aligned} u &= (1-\delta)(\omega r \sin\theta - U_1) \\ v &= (1-\delta)\omega r \cos\theta \end{aligned}\right\},\ R_P \le r \le R_S \tag{22}$$

3.2. Material properties

The density of AA7075 and AA6061 is taken as constant, equals to 2810 kg/m^3 and 2700 kg/m^3 respectively, while the specific heat and thermal conductivity are considered as temperature dependent properties [34] as given below

$$k = 25.2 + 3.98 \times 10^{-1} T + 7.36 \times 10 - 6T^2 - 2.25 \times 10^{-7} T^3$$
$$C_P = 929 - 6.27 \times 10^{-1} T + 1.48 \times 10 - 3T^2 - 4.33 \times 10^{-8} T^3$$

3.3. Residual stress measurement by cosα method

A mini portable X-ray diffraction apparatus (pulstec μ-X360) used for analyzing the residual stresses in welded joint of AA6061 and AA7075 samples. The X-ray incident angle was set 35° and ±5° oscillation was applied. The X-ray incident time was 4–5 min throughout this process for each sample. Under these conditions, a diffracted beam from the workpiece surface has captured the

images of the welded plates at 50 μm resolution, the size of the beam spot is approximately 2.5 mm for 1.2 mm pinhole collimator.

For residual stress determination, the cosα method was described [35]. The translation from the diffractometer space to the sample inherently more complex due to the 2D planar geometry of the measurement and can be expressed as

$$q_s = \begin{bmatrix} \cos\eta \sin\psi_0 + \sin\eta \cos\psi_0 \cos\alpha \\ \cos\eta \sin\psi_0 \sin\varphi_0 + \sin\eta \cos\psi_0 \sin\varphi_0 cos\alpha + \sin\eta \cos\varphi_0 \sin\alpha \\ \cos\eta \cos\psi_0 + \sin\eta \sin\psi_0 cos\alpha \end{bmatrix} \tag{23}$$

The strain projection along (η, α) coordinates can be written as in terms of scattering vector and strain component as

$$\begin{aligned} \varepsilon_\alpha &= q_i \cdot q_j \cdot \varepsilon_{ij} \\ \varepsilon_{ij} &= \frac{1+\nu}{E}\sigma_{ij} - \delta_{ij}\frac{\nu}{E}\sigma_{kk} \end{aligned} \tag{24}$$

So, the strain projection may be written as

$$\varepsilon_\alpha = \frac{1+\nu}{E} q_i q_j \sigma_{ij} - \frac{\nu}{E}\sigma_{kk} \tag{25}$$

Now, defining two parameters a_1 and a_2 for linear determination of σ_{11} and σ_{22}

$$a_1 = \frac{1}{2}[(\varepsilon_\alpha - \varepsilon_{\pi+\alpha}) + (\varepsilon_{-\alpha} - \varepsilon_{\pi-\alpha})] \tag{26}$$

$$a_2 = \frac{1}{2}[(\varepsilon_\alpha - \varepsilon_{\pi+\alpha}) - (\varepsilon_{-\alpha} - \varepsilon_{\pi-\alpha})] \tag{27}$$

After re-expressing of Eq. (26) and Eq. (27) to lead the final relationship for this method.

$$\begin{aligned} a_1 = \frac{1+\nu}{E}\sin\psi_0 \sin 2\eta \cos\alpha [\sigma_{11}(1+\cos 2\varphi_0) \\ + \sigma_{22}(1-\cos 2\varphi_0) + 2\sigma_{12}(\sin 2\varphi_0)] \end{aligned} \tag{28}$$

$$\begin{aligned} a_2 = \frac{1+\nu}{E}\sin\psi_0 \sin 2\eta \sin\alpha [\sigma_{22} \sin 2\varphi_0 - \sigma_{11} \sin 2\varphi_0 \\ + 2\sigma_{12} \cos 2\varphi_0] \end{aligned} \tag{29}$$

at $\varphi_0 = 0$, the above equations will be

$$a_1 = \sigma_{11}\frac{1+\nu}{E}\sin 2\psi_0 \sin 2\eta \cos\alpha \tag{30}$$

$$a_2 = 2\sigma_{12}\frac{1+\nu}{E}\sin\psi_0 \sin 2\eta \sin\alpha \tag{31}$$

Thus the term cosα in Eq. (30) is the origin of the name for this method.

The value of stresses after re-expression maybe written as

$$\sigma_{11} = -\frac{E}{(1+\nu)} \frac{1}{\sin 2\psi_0 \sin 2\eta} \tag{32}$$

$$\sigma_{12} = -\frac{E}{2(1+\nu)} \frac{1}{\sin 2\psi_0 \sin^2\eta} \tag{33}$$

4. Results and discussion

4.1. Tensile strength

In order to analyze the effect of friction stir processing on the TIG-welded joint, the tensile load applied on TIG and TIG+FSP welded joint by universal testing machine (UTM) at room temperature and fractured surfaces obtained from the tensile test were compared with one another. Three test specimens were tested at each condition and the average of these three results are presented in Tables 4–10. The tensile strength of the weldment made by TIG and TIG+FSP techniques are compared. Due to the absence of porosity, small grain size and presence of extra material in the welded region with filler wire, the tensile strength of TIG+FSP obtained higher value than the conventional TIG joining process. Filler ER5356 present in the welded joint makes more compact pressure leading to increase bond strength instead of filler ER4043. The grain size in the fusion zone for ER5356 is smaller than the ER4043. The tensile strength with filler ER5356 was obtained higher than ER4043 [36]. According to Hall Petch equation $\sigma_1 = \sigma_i + kd^{(-1/2)}$, the tensile strength is inversely proportional to the grain size [37]. The tensile strength of the TIG-welded joint using filler 4043 and 5356 was calculated 158.6 MPa and 172.2 MPa respectively which is less than the TIG+FSP as shown in Table 4. The tensile strength of the TIG+FSP welded joint increased with increasing tool rotational speed. The highest tensile strength (233.17 MPa) was observed in TIG+FSP with filler ER5356 at tool rotational 1600 rpm with feed rate 63 mm/min. Three statistical parameters are investigated i.e., standard deviation (SD), standard error (SE) and 95% confidence interval for TIG+FSP welded joint with filler ER4043 and ER5356 as shown in Tables 5–10. The standard deviation (SD) provides the deviance of the experimental

Table 4
Mechanical properties of TIG welded joint.

Processing Parameters	Tensile Strength/MPa	Hardness/HV	Residual stress/MPa
TIG with filler ER4043	158.6	66	71
TIG with filler ER 5356	172.2	74	67

Table 5
Tensile strength of TIG+FSP welded joint with filler ER4043.

Processing Parameters	Tensile Strength/MPa			Mean Tensile Strength/MPa	Standard Deviation	Standard error	95% confidence Interval	
	Specimen-1	Specimen-2	Specimen-3				Minimum	Maximum
TIG+FSP_800	178.4	178.0	178.8	178.40	0.40	0.23	177.95	178.85
TIG+FSP_1000	189.0	189.4	190.4	189.60	0.72	0.42	188.78	190.42
TIG+FSP_1250	204.5	204.8	205.0	204.77	0.25	0.15	204.48	205.05
TIG+FSP_1600	219.0	219.6	220.0	219.53	0.50	0.29	218.96	220.10

Table 6
Hardness of TIG+FSP welded joint with filler ER4043.

Processing Parameters	Hardness/HV			Mean Hardness /HV	Standard Deviation	Standard error	95% confidence Interval	
	Specimen-1	Specimen-2	Specimen-3				Minimum	Maximum
TIG+FSP_800	82.5	82.0	83.5	82.6	0.76	0.44	81.80	83.53
TIG+FSP_1000	89.0	90.0	89.0	89.3	0.58	0.33	88.68	89.99
TIG+FSP_1250	92.6	92.0	92.0	92.2	0.35	0.20	91.81	92.59
TIG+FSP_1600	96.0	97.0	96.5	96.5	0.50	0.29	95.93	97.07

Table 7
Residual Stress of TIG+FSP welded joint with filler ER4043.

Processing Parameters	Residual Stress/MPa			Mean Residual Stress/MPa	Standard Deviation	Standard error	95% confidence Interval	
	Specimen-1	Specimen-2	Specimen-3				Minimum	Maximum
TIG+FSP_800	63	63	64	58.67	0.58	0.33	58.01	59.32
TIG+FSP_1000	59	58	57	56.33	1.00	0.58	55.20	57.46
TIG+FSP_1250	49	50	49	51.00	0.58	0.33	50.35	51.65
TIG+FSP_1600	43	43	45	44.67	1.15	0.67	43.36	45.97

Table 8
Tensile strength of TIG+FSP welded joint with filler ER5356.

Processing Parameters	Tensile Strength/MPa			Mean Tensile Strength/MPa	Standard Deviation	Standard error	95% confidence Interval	
	Specimen-1	Specimen-2	Specimen-3				Minimum	Maximum
TIG+FSP_800	187.5	187.0	187.6	187.37	0.32	0.19	187.00	187.73
TIG+FSP_1000	194.2	194.8	195.4	194.80	0.60	0.35	194.12	195.48
TIG+FSP_1250	218.4	219.4	218.8	218.87	0.50	0.29	218.30	219.44
TIG+FSP_1600	233.0	233.5	233.0	233.17	0.29	0.17	232.84	233.49

Table 9
Hardness of TIG+FSP welded joint with filler ER5356.

Processing Parameters	Hardness/HV			Mean Hardness /HV	Standard Deviation	Standard error	95% confidence Interval	
	Specimen-1	Specimen-2	Specimen-3				Minimum	Maximum
TIG+FSP_800	89.5	89.0	89.0	89.2	0.29	0.17	88.84	89.49
TIG+FSP_1000	93.0	94.5	94.0	93.8	0.76	0.44	92.97	94.70
TIG+FSP_1250	99.5	99.0	100.0	99.5	0.50	0.29	98.93	100.07
TIG+FSP_1600	102.0	102.0	102.5	102.2	0.29	0.17	101.84	102.49

Table 10
Residual Stress of TIG+FSP welded joint with filler ER5356.

Processing Parameters	Residual Stress/MPa			Mean Residual Stress/MPa	Standard Deviation	Standard error	95% confidence Interval	
	Specimen-1	Specimen-2	Specimen-3				Minimum	Maximum
TIG+FSP_800	58	58	60	58.7	1.15	0.67	57.36	59.97
TIG+FSP_1000	52	53	52	52.3	0.58	0.33	51.68	52.99
TIG+FSP_1250	39	38	40	39.0	1.00	0.58	37.87	40.13
TIG+FSP_1600	32	31	32	31.7	0.58	0.33	31.01	32.32

values from the mean it may be calculated as $SD = [\Sigma(X_i - M)^2/(N-1)]^{1/2}$ and the standard error is a quantity used to measure how to close the prediction values to the experimental values. *SE* is calculated as $SE = SD/N^{1/2}$, where N= No of observation and M = mean.

The confidence interval has shown that tensile strength and hardness increased with increasing tool rotation, whereas residual stress decreased with increasing tool rotation.

4.2. Micro-hardness

The micro-hardness distribution of the TIG-welded joint of AA6061 and AA7075 with different filler wire and TIG+FSP weldments with different processing parameters were analyzed by Vickers hardness testing results are shown in Fig. 4. Vicker microhardness machine was used for measuring the hardness across the welded joints with a load of 100 g and dwell time 30 s. The hardness distributions are asymmetrical in the weld center due to the microstructure of the advancing side and retreating side introduced by unsteady plastic flow from the base metal to the weld center [38–40]. The hardness slopes downward from the base metal to the welded region. The hardness fluctuates largely on the advancing side while the hardness holds steady in the retreating side [41].

The alloying elements such as Si and Mg existing in the weld center make precipitation reaction and form a strong precipitate of Mg_2Si to give a higher strength as shown in Fig. 5(a). Fig. 4 shows the micro-hardness profile at the heat-affected zone of aluminum alloy 6061 and 7075. It showed a significant difference, where the

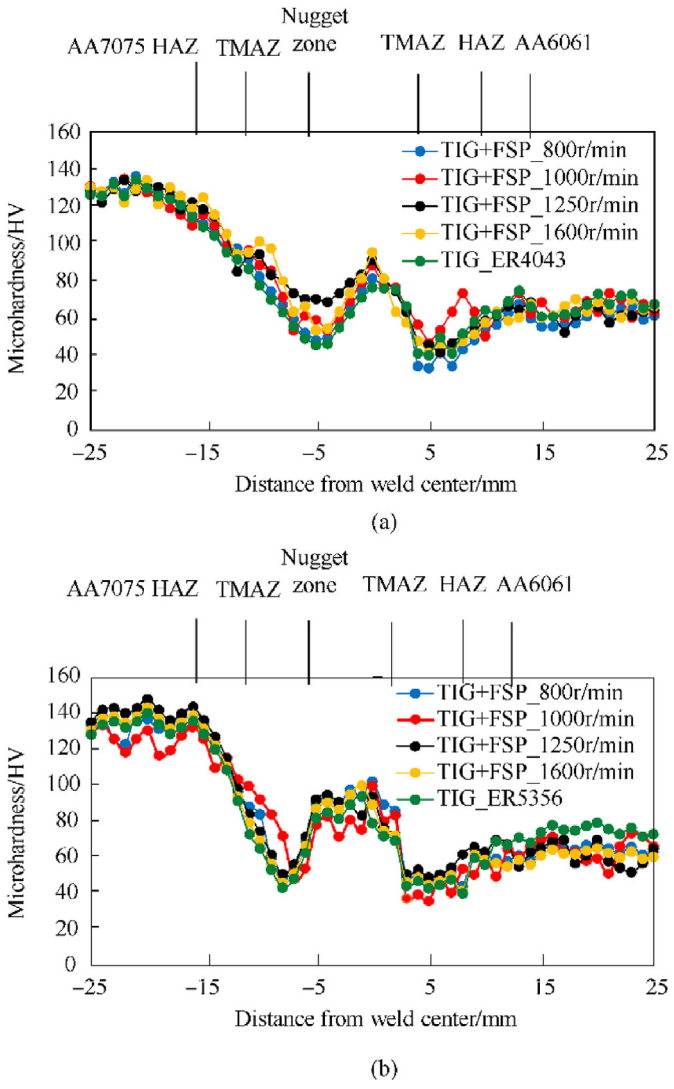

Fig. 4. Comparison of micro-hardness of TIG and TIG+FSP, (a) filler wire ER4043, (b) filler wire ER5356.

welded joint using filler ER4043 showed a lower average hardness value compared to filler ER5356. The hardness value at the center of weldment for filler ER4043 and ER5356 are 96 HV and 102 HV respectively, during welding, the filler wire ER4043 shows the columnar grains while fine equiaxed grains are found in ER5356. It may be analyzed that the fine equiaxed grains improve mechanical properties than the columnar grains [42].

4.3. XRD and EDX analysis

X-ray diffraction (XRD) analysis has been taken on transverse cross-sections of dissimilar TIG and TIG+FSP welded joint of AA6061 and AA7075 with filler ER4043 and ER5356. The corresponding pattern for the welded joints are shown in Fig. 5 and found four major phases i.e. Al, Al_2CuMg, $MgZn_2$, and Mg_2Si. Magnesium (Mg) and Silicon (Si) elements were found in the weldment besides the aluminum (Al), it is found that Mg and Si created the phase after the precipitation reaction in the weldment. The very high intensity was found from aluminum, because of the fragmentation of precipitates the intensity of $MgZn_2$ was decreases after friction stir processing on TIG welded joint with filler ER5356. The alloying elements such as Si and Mg existing in the weld center make precipitation reaction and form a strong precipitate of Mg_2Si to give a higher strength. The same phase of Al_2CuMg was detected in both the cases (filler ER4043 and ER 5356).

The hardness of the FSP joints is based on boundary energy, brittle intermetallic formation, strain hardening and precipitates formation in the joint. Fine recrystallized grains and increase of grain boundaries in the (SZ) of AA6061 and AA7075 joints predict higher hardness. Because of fine precipitates and fine grains structure, the stir zone is associated with plastic deformation and high temperature, due to precipitates formation at high temperature along the grain boundaries the hardness value of TIG+FSP at 1600 rpm with filler ER5356 recorded higher values than the TIG welded joints. The energy-dispersive X-ray spectroscopy (EDX/EDS) of the TIG-welded joint with filler ER4043 and ER 5356 welded joint has been analyzed. It was found that the atomic percentage of Si and Mg in the welded joint is higher than the other elements. Fig. 5(b) and (c) illustrates the EDX image and percentage of element concentration at fusion zone (FZ) in the TIG welded joint with filler ER4043 and ER5356. Zinc (Zn), Magnesium (Mg) and Silicon (Si) elements were found in the weldment besides the aluminum (Al), it is found that Mg, Zn, and Si created the phases after the precipitation reaction in the weldment.

4.4. Residual stresses measurement

A mini portable X-ray diffraction apparatus (Pulstec μ-X360) at Delhi technological university, Delhi, India was used to determine the residual stresses in weldment of AA6061 and AA7075 by the cosα method. The cosα method was introduced in japan for residual stress analysis in 1978 [43]. This method is allowed the stress analysis by capturing the results by a single incident X-ray beam via a 2D detector. It shows the peak center is very stable throughout the welding. Debye ring and distortion ring is obtained by using cosα method. An investigation has been done to analyze the residual stress. The 3D Debye ring and distortion ring of welded samples are shown in Fig. 7. The X-ray incident angle was set 35° and ±5° oscillation was applied. The variation of residual stresses in the transverse direction of weldment with filler ER4043 and ER5356 are shown in Fig. 6(a) and (b). Residual stresses (compressive or tensile) will influence the mechanical behavior of the welded joint. It can reduce brittle fracture strength, buckling strength and cracking in the weldment. Residual stress is also influenced by the prediction of brittle failure and affect the lifetime prediction of the component [44–47]. Residual stress contributes both negative and positive effects to the weldment, generally, the tensile residual stress leads to a negative effect on the weldment [48]. When the fixtures are unconstrained and the welded plate temperature is reduced to room temperature, the material in the nugget zone (NZ) tends to recover, but the material in the heat-affected zone (HAZ) has smaller deformation and will prevent the recovery process in NZ, so the maximum residual stress occurs in the boundaries of the HAZ with a minimum in the NZ. The deformation on the advancing side and retreating side differ, causing the recovery processes to differ too. So the residual stress cannot be symmetry to the welding line [49]. The base material AA7075 on LHS of the weldment shows a minimum compressive residual stress, however, the residual stress gradually increases from the base material to towards the weldment and then decreases till second base material AA6061. The maximum residual stress occurs in the location where the equivalent of the plastic strain is decreased suddenly. The maximum compressive residual stress 71 MPa were located at the fusion zone (FZ) of the TIG weldment with filler ER4043, whereas minimum compressive residual stress 37 MPa was obtained at stir zone (SZ) of the TIG+FSP with filler 5356, the residual stresses profile of TIG+FSP were not symmetrical about the centerline of the

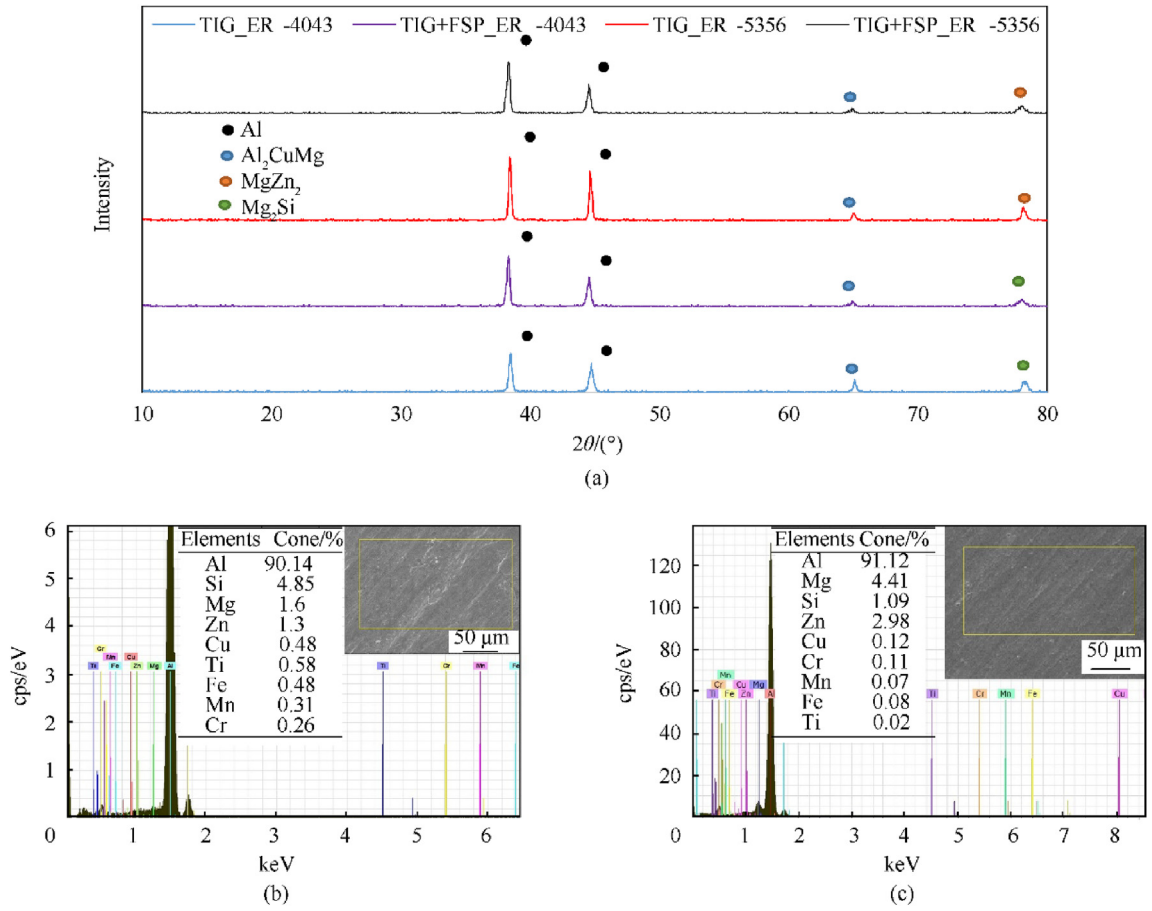

Fig. 5. (a) XRD peaks of TIG and TIG+FSP welded joint, (b&c) EDX analysis of TIG welded joint in fusion zone with filler ER4043 and filler ER 5356.

weldment for both the cases. The left side peak value of the weldment was greater than the right side because the forming processes are different for the retreating side (RS) and advancing side (AS).

4.5. Model validation

To confidently use CFD results for investigating the TIG+FSP process, the CFD model has to be correctly defined and a thorough validation has to be achieved. The model was first applied to simulate the experimental work on friction stir welded joint of Al-alloy 6061 carried out by Hwang el al [50]. The experimental temperatures were measured by thermocouple units placed equally at a distance of 5 mm, along the traverse direction of the rotating tool. The tool rotational speed and traverse speed, was 920 rpm and 20 mm/min respectively. The present simulation result was validated by this experimental results which gives the satisfactory amount of assurance in the fidelity of the simulation of welded joints as shown in Table 11.

4.6. Temperature variation in TIG+FSP process

The experimental temperature results of TIG+FSP measured by thermocouples. The advancing side temperatures in the transverse direction are A_1, A_2, A_3, and A_4 and the retreating side has R_1, R_2, R_3, and R_4. The peak temperature of advancing side is marginally higher than the retreating side [51,52]. The temperature of FSP tool is symmetric about the tool axis. The high temperature in the vicinity of the welding tool is attributed to the localized heat generation. During the TIG+FSP process, the temperature of the base plate around the welding tool is around the 765 K. It is still lower than the melting point of AA6061 and AA7075. When the position weld bead is far away from the FSP tool, the temperature drops quickly as shown in Fig. 9(a) and (b). Fig. 8 shows the temperature distribution plot for TIG+FSP welding at 160 s. During this simulation, eight points were observed to obtain the temperature-time curves which can be compared with the experimental results. The area around the FSP tool reached the maximum temperature. The maximum temperature was observed 760 K at the advancing side whereas minimum temperature was observed 307 K at the retreating side. Higher heat is generated in the SZ at high tool rotation, the prevailing thermal conditions are controlled by the distribution and availability of precipitates in the matrix. Fig. 10 shows the temperature variation profile on the mid-section of the top surface of (TIG+FSP) welded joint with different processing parameters. The region where its peak temperature is higher almost 450 °C in (TIG+FSP) of AA6061 and AA7075 aluminum alloy at tool rotational speed of 1600 rpm. The heat is transmitted to the aluminum alloy which is preheated during tool rotation. The initial heating was predicted as the monitoring thermal contour of the rotating tool. When the rotating tool moves on the monitoring location, the temperature contour leads to slow cooling. Due to the relation between tool pin rotation and material flow, the higher shearing rate was observed at (A.S). Thus the temperature of (RS) is slightly lower than the (AS), while almost the symmetric temperature was observed at the bottom of the welded joint.

The estimated maximum temperature about 515 °C was calculated in the stir zone of the TIG+FSP welded joint at tool rotation of

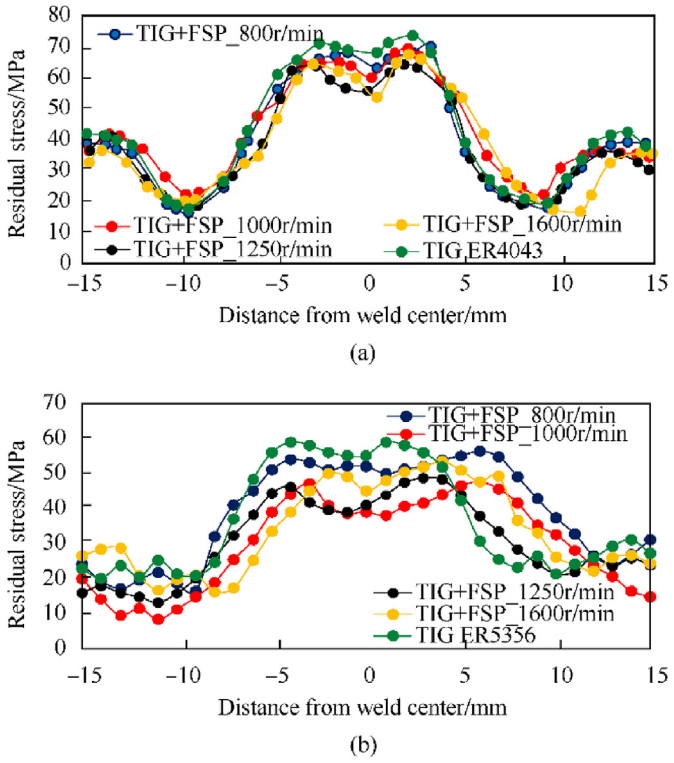

Fig. 6. Variation of transverse compressive residual stress at the welded joint, (a) filler ER4043, (b) filler ER5356.

1600 rpm whereas 408 °C was calculated in the stir zone at 800 rpm. The temperature and heat flux distribution with different processing parameters are shown in Figs. 10 and 11. In general, the temperature values at the (A.S) about 10–25 °C greater than the

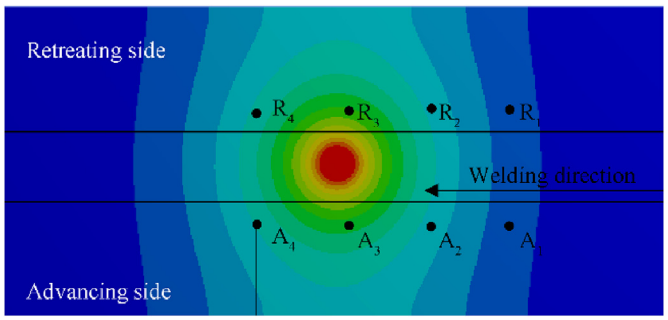

Fig. 8. Temperature contour of TIG+FSP at 160 s.

(R.S), When the tool approaches the target location then there is a rapid change in the temperature, while the slower cooling rate was observed when the tool moves away from the target location [53]. The variation of heat flux at the tool workpiece interface is shown in Fig. 11. It was observed that the heat flux is directly proportional to the tool rotational speed. The maximum heat flux about 5.33×10^6 w/m^{2}was obtained in the SZ at 1600 rpm, whereas minimum heat flux was obtained at 1000 rpm. The non-uniformity was observed in the heat flux pattern at different processing parameters of the tool, because the rapid recirculation of plasticized material, the heat flux rate does not lead to the variation of local temperature.

4.7. Microstructure analysis of TIG and TIG+FSP welded joint

For metallography observation, samples were first ground and mechanically polished and then etched in keller reagent (HNO_3, HF and HCL) and observed by the microscopic machine. The microstructure of TIG welded joint of Al-6061 and 7075 with filler ER4043 and ER 5356 were observed at fusion zone as shown in

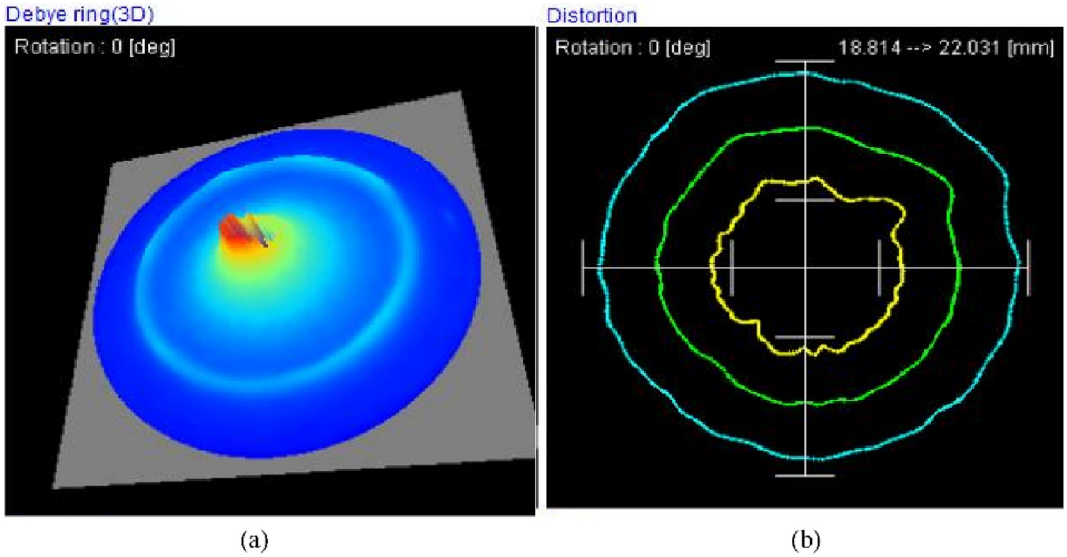

Fig. 7. (a) 3D Debye ring at the center of the TIG+FSP welded joint, (b) 2D Distortion ring at the center of the TIG+FSP welded joint.

Table 11
Validation of temperature distribution of friction stir welded joint of AA6061 [50].

Author	Rotation speed/rpm	Traverse speed/(mm·min^{-1})	Maximum temperature/°C
Present result	920	20	398
Hwang et al. [50]	920	20	386

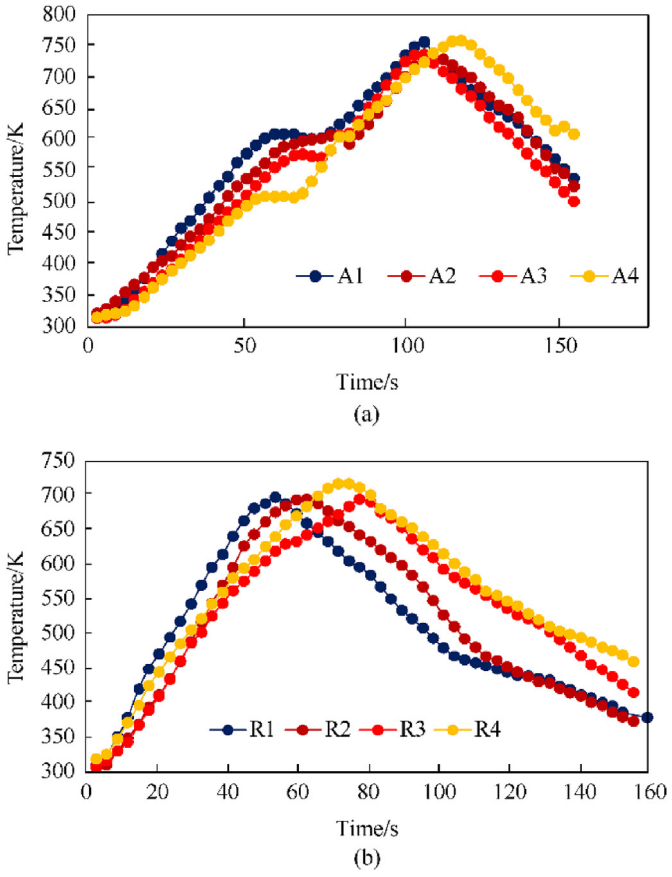

Fig. 9. Variation of temperature during TIG+FSP welding: (a) Advancing side, (b) Retreating side.

Fig. 12. The dispersed precipitates of Al_2CuMg intermetallic compound were observed in welded region and coarse equiaxed grains were also observed in fusion zone with filler ER4043. The equiaxed grains is absent due to the material close to the fusion line provides plenty of sources for the crystal nucleation of the liquid metal during the TIG welding [54]. Fine grains with small precipitates was reported in TIG welded joint with filler ER5356 as compare to ER4043.

Three different zones have been recognized in TIG+FSP weldment at low magnification due to mechanical and thermal stresses caused by the processing parameters. These zones are nugget zone (NZ), thermo-mechanically affected zone (TMAZ), and heat affected zone (HAZ). The formation of nugget zone shape in TIG+FSP welded joint is recognized to the maximum deformation and plasticization in the material which shows the fine recrystallized equiaxed grains. The formation of nugget shapes depends on thermal gradient, processing parameters and tools geometry in the work-piece [55]. Therefore, coarse grain structure of TIG welded joint is transformed into the uniform and fine grains structures in the weld nugget zone due to adequate softening of material revealed the maximum tensile strength and microhardness of the TIG+FSP welded joint as shown in Fig. 13. At high welding speed, the weld nugget zone is more homogenous than those produce low welding speed because high heat input gives the effective recrystallization and more homogenous temperature distribution in weld nugget zone. The grains size in stir zone change crucially which is depend on the heat input and processing parameters [56,57].

The grain size of TIG weldment were analyzed by the image J software and observed grain size in fusion zone with filler ER4043 and ER5356 are 20.4 μm, and 18.2 μm. Fig. 14 shows the effect of tool rotational speed on grain size of TIG+FSP welded joint at nugget zone. It can be conclude that the rotational speed has a significant effect of grain size of the welded joint. When the rotational speed increases, grain size decreases, this observation give the satisfactory amount of assurance with Yupeng Li [58]. The average minimum grain size i.e. 3.4 μm was observed in TIG+FSP with filler ER5356 at tool rotational speed 1600 rpm.

Fig. 15 shows the fractured surface after the tensile test. In this analysis two mode of failure were observed. The fractured occurs in retreating side at low rotational speed (800 rpm), on the other hand failure was observed in advancing side at high tool rotational speed (1600 rpm). This observation gives the satisfactory amount of assurance with Mishra [5]. SEM fractograph has been taken from the fractured tensile test. fracture morphology between the TIG and TIG+FSP shows that TIG welded portion shows the large voids whereas TIG+FSP welded portion shows fine dimples, this is the evidence of crack nucleation and growth 4 mm away from the weld line. The ductile fracture of welded joint occurs, an improvement in

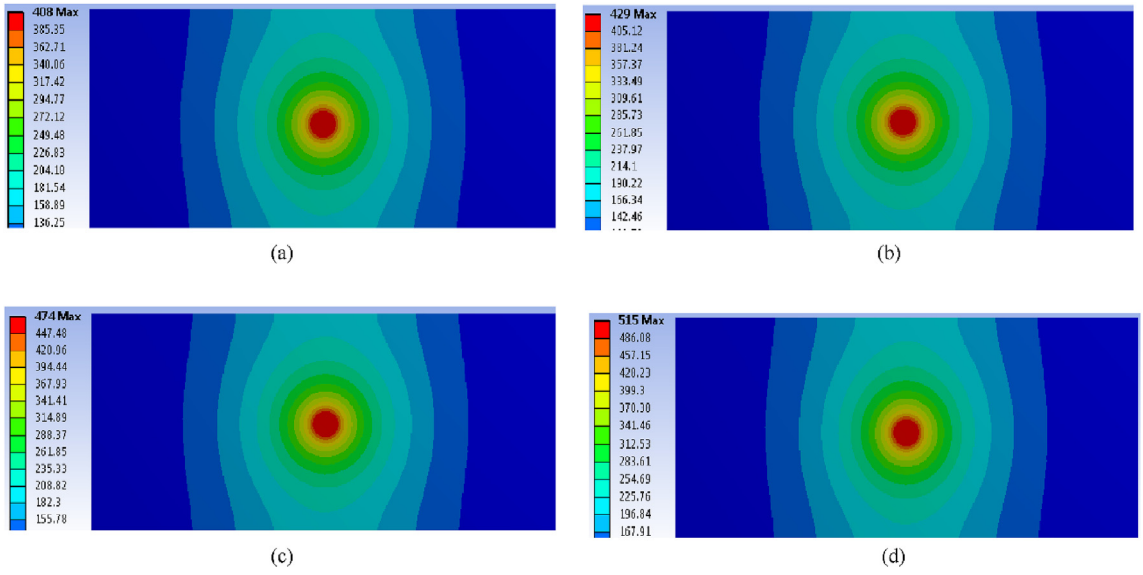

Fig. 10. Temperature distribution at the center of the TIG+FSP welded joint, (a) 800 rpm, (b) 1000 rpm, (c) 1250, (d) 1600 rpm.

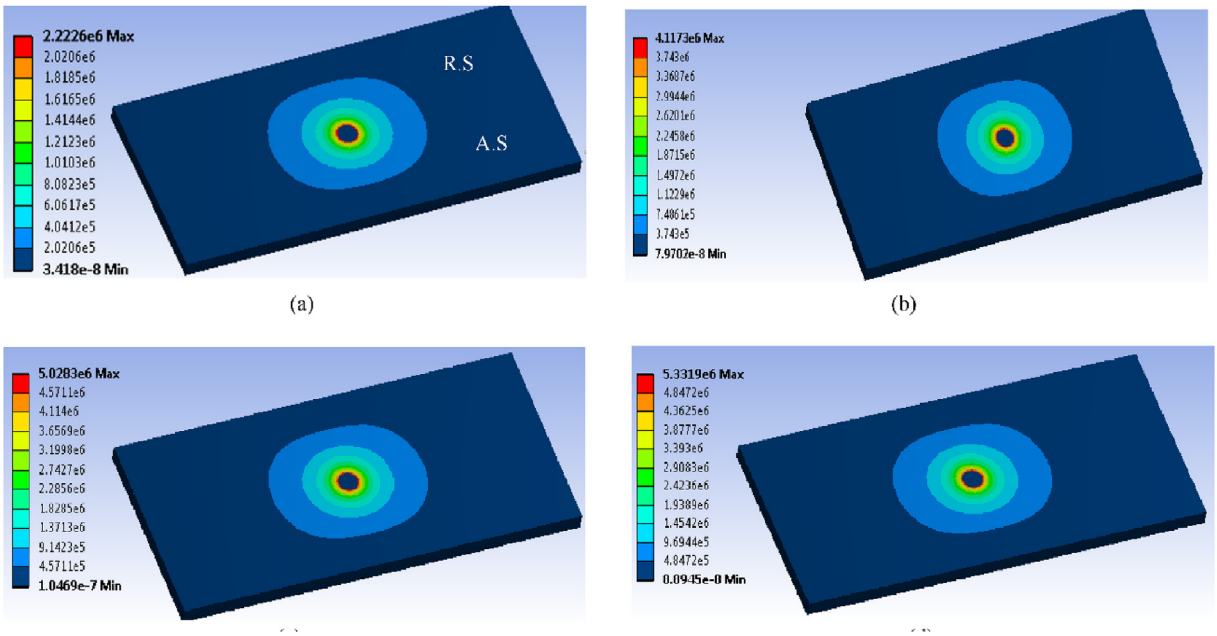

Fig. 11. The heat flux at the center of TIG+FSP welded joint, (a) 800 rpm, (b) 1000 rpm, (c) 1250 rpm, (d) 1600 rpm.

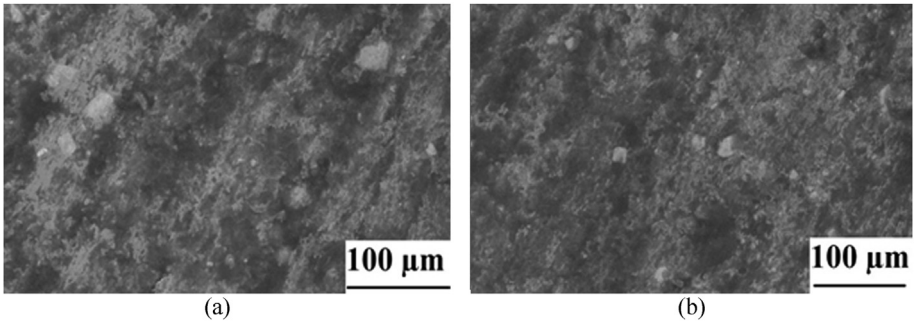

Fig. 12. SEM images of TIG welded joint at fusion zone (a) filler ER 4043, (b) filler ER 5356.

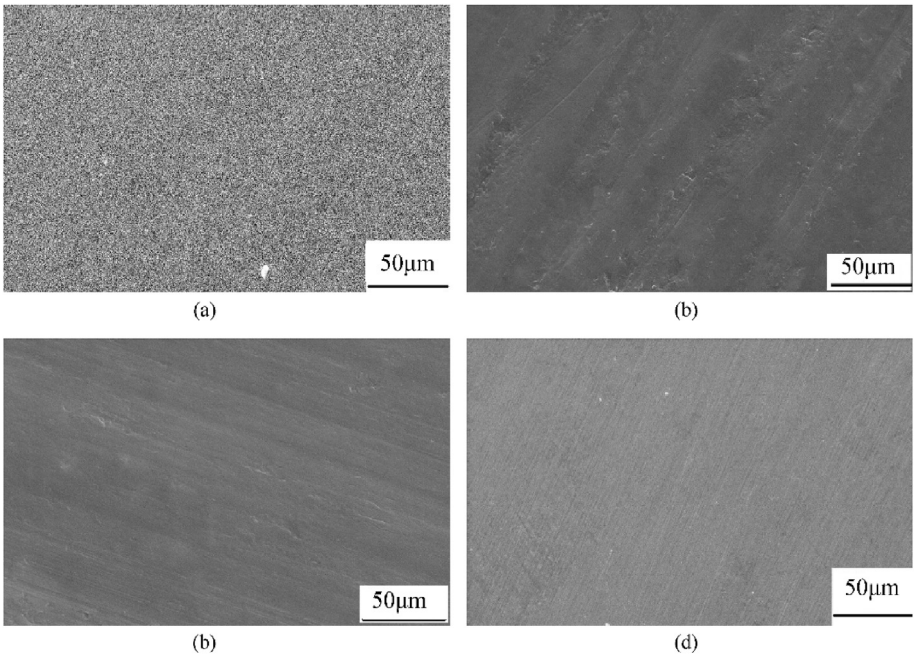

Fig. 13. SEM images of TIG+FSP welded joint at tool rotation (a) 800 rpm, (b) 1000 rpm, (c) 1250 rpm, (d) 1600 rpm.

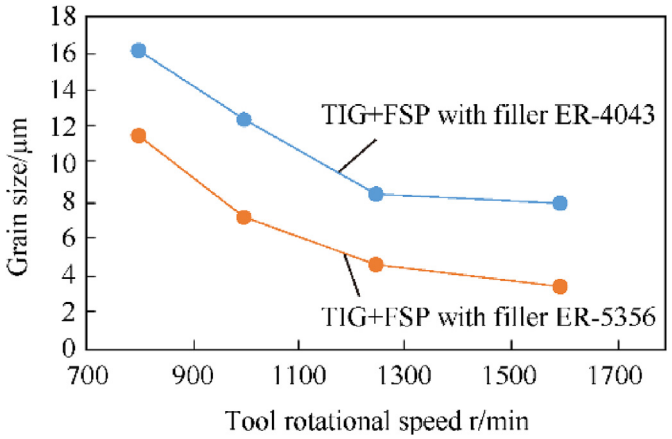

Fig. 14. Effect of tool rotational speed on grain size of TIG+FSP welded joint.

ductility may be achieved when the cavity nucleation could be suppressed [59]. The maximum inter-facial normal stress is depends upon the grain particle size and the volume fraction of the grain particles [60]. The fractured surface at room temperature were shown in Fig. 15.

The large dimples and quasi cleavage with sharp edge and various depth were found on the fractured tensile specimen surface of TIG welded joint with filler ER4043 and ER5356as shown in Fig. 15(a) and (b). Many large and equiaxed dimples were observed in TIG welded joint with filler ER4043 whereas the main fractured mode was quasi cleavage with lot of tiny dimples gathered around the large and quasi cleavage dimples found in filler ER5356 which shows the ductile fracture. The FSW processing parameters effect the temperature distribution and material flow across the TIG welded joint. Fig. 15(c) shows the SEM micrograph of factored surface of TIG+FSP welded joint, finer dimples are observed in TIG+FSP weldment as compare to TIG welded joint, which shows the better mechanical properties.

5. Conclusion

A new welding approach has been investigated to see the effect of FSP on TIG welding for dissimilar alloy AA6061 and AA7075 followed by the different filler wire ER4043 and ER5356. The mechanical characterization, finite element formulation and mathematical equations of heat transfer of TIG+FSP welded joints are investigated using ANSYS Fluent software by adjusting process parameters of FSP. The confidence interval has shown that tensile strength and hardness increased with increasing tool rotation, whereas residual stress decreased with increasing tool rotation. The maximum compressive residual stress 71 MPa were located at the fusion zone (FZ) of the TIG weldment with filler ER4043, whereas minimum compressive residual stress 37 MPa was obtained at stir zone (SZ) of the TIG+FSP with filler 5356. The large dimples and quasi cleavage with sharp edge and various depth were found on the fractured tensile specimen surface of TIG welded joint with filler ER4043 and ER5356 whereas fine dimples are observed in TIG+FSP weldment, which shows the better mechanical properties. TIG+FSP resulted in generated fine grains of 3.2–4 μm. The grain size decreases by increasing the tool rotational speed. The minimum grain size was obtained in TIG+FSP welded joint with filler ER5356 at 1600 rpm.

The asymmetry of the temperature distribution during TIG+FSP welding of AA7075 and AA6061 determined by numerical simulation corresponded with the experimental results. The peak temperatures on AS were higher than the RS of 20 K. The heat transfer is

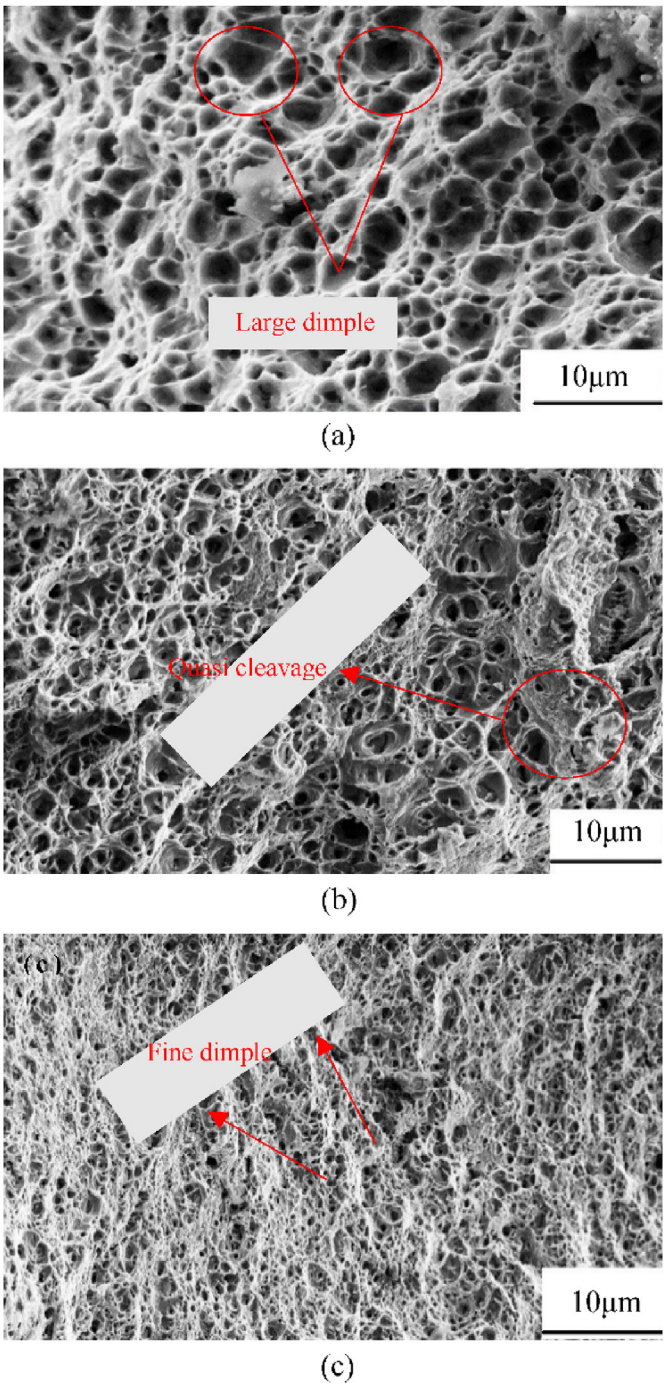

Fig. 15. SEM images of fractured tensile specimen, (a) TIG welded joint with filler ER4043, (b) TIG welded joint with filler ER4043, (c) TIG+FSP welded joint.

analyzed by the effect of different processing parameters of FSP tool. The temperature at advancing side is higher than the retreating side. The predicted peak values of temperature at the weld region was calculated by the ANSYS software and found the maximum temperature about 515 °C at tool rotation of 1600 rpm, whereas the maximum heat flux rate about 5.33×10^6 was observed at 1600 rpm.

Declaration of competing interest

The author declare that they have no conflict interest.

References

[1] Dialami N, Chiumenti M, Cervera M, de Saracibar CA. Challenges in thermo-mechanical analysis of friction stir welding processes. Arch Comput Methods Eng 2017b;24:189–225.
[2] Gemme F, Verreman Y, Dubourg L, Jahazi M. Numerical analysis of the dwell phase in friction stir welding and comparison with experimental data. Mater Sci Eng A 2010;527(16):4152–60.
[3] Mosneaga VA, Mizutani T, Kobayashi T, Toda H. Impact toughness of weldments in Al-Mg-Si alloys. Mater Trans 2002;43:1381–9.
[4] Karunakaran N. Effect of pulsed current on temperature distribution and characteristics of GTA welded Magnesium alloy, vol. 4; 2013. p. 1–8.
[5] Mishra RS, Ma ZY. Friction stir welding and processing. Mater Sci Eng R Rep 2005;50(1):1–78.
[6] Zhan M, Guo K, Yang H. Advances and trends in plastic forming technologies for welded tubes. Chin J Aeronaut 2015;29(2):305–15.
[7] Masubuchi K. Analysis of welded structures, residual stresses, distortion, and their consequences. New York: Pergamon Press; 1980.
[8] Chen G-Q, Shi Q-Y, Li Y-J, Sun Y-J, Dai Q-L, Jia J-Y, Zhu Y-C, Wu J-J. Computational fluid dynamics studies on heat generation during friction stir welding of aluminum alloy. Comput Mater Sci 2013;79:540–6.
[9] Su H, Wu CS, Pittner A, Rethmeier M. Thermal energy generation and distribution in friction stir welding of aluminum alloys. Energy 2014;77:720–31.
[10] Nandan R, Roy GG, Lienert TJ, Debroy T. Three-Dimensional heat and material flow during friction stir welding of mild steel. Acta Mater 2007;55(3):883–95.
[11] Ji S, Shi Q, Zhang L, Zou A, Gao S, Zan L. Numerical simulation of material flow behavior of friction stir welding influenced by rotational tool geometry. Comput Mater Sci 2012;63:218–26.
[12] Yu Z, Zhang W, Choo H, Feng Z. Transient heat and material flow modeling of friction stir processing of Magnesium alloy using threaded tool. Metall Mater Trans A 2012;43(2):724–37.
[13] Su H, Wu CS, Bachmann M, Rethmeier M. Numerical modeling for the effect of pin profiles on thermal and material flow characteristics in friction stir welding. Mater Des 2015;77:114–25.
[14] Dalle Donne C, Biallas G, Ghidini T, Raimbeaux G. Effect of weld imperfections and residual stresses on the fatigue crack propagation in friction stir welded joints. In: 2nd international conference on friction stir welding. Gothenburg, Sweden; 2000.
[15] Dalle Donne C, Lima E, Wegener E, Pizalla A, Buslaps T. Investigations on residual stresses in friction stir welds. In: 3rd international conference on friction stir welding, Kobe, Japan; 2001.
[16] Peel M, Steuwer A, Preuss M, Withers PJ. Withers, microstructure, mechanical properties and residual stresses as a function of welding speed in aluminum AA5083 friction stir welds. Acta Mater 2003;51(16):4791–801.
[17] Wang X-L, Feng Z, David SA, Spooner S, Hubbard CR. In: 6th int. Conf. Residual stresses, Oxford, UK, July 10-12; 2000.
[18] Cao YJ, Qi X. Thermal and thermo-mechanical modeling of friction stir welding of aluminium alloy 6001-T6. J Mater Process Manuf Sci 1998;7:215–33.
[19] Chen CM, Kovacevic R. Finite element modeling of friction stir welding-thermal and thermomechanical analysis. Int J Mach Tool Manufact 2003;43:1319–26.
[20] Zhu XK, Chao YJ. Numerical simulation of transient temperature and residual stresses in friction stir welding of 304L stainless steel. J Mater Process Technol 2004;146:263–72.
[21] Li T, Shi Q-Y, Li H-K, Wang W, Cai Z-P. In: Proc. Int. Weld. Join. Conf. Seoul, Korea: COEX Convention Center; May 2007.
[22] Sutton MA, Reynolds AP, Wang DQ, Hubbard CR. J Eng Mater Technol 2002;124(4):215–21.
[23] Mehdi Husain, Mishra RS. Mechanical properties and microstructure studies in friction stir welding (FSW) joints of dissimilar alloy-A review. J Achiev Mater Manuf Eng 2016;77(1):31–40.
[24] Mehdi Husain, Mishra RS. Influences of process parameter and microstructural studies in friction stir welding of diferent alloys: a review. Int J Adv Prod Ind Eng 2017;509:55–62.
[25] Mehdi Husain, Mishra RS. Mechanical and microstructure characterization of friction stir welding for dissimilar alloy—a review. Int J Res Eng Innov 2017;1(5):57–67.
[26] Mehdi Husain, Mishra RS. Analysis of material fow and heat transfer in reverse dual rotation friction stir welding: a review. Int J Steel Struct 2019;19:422–34.
[27] Husain Mehdi H, Mishra RS. Study of the influence of friction stir processing on tungsten inert gas welding of diferent aluminum alloy. SN Appl Sci 2018;1:712. 2019.
[28] Taheri-Behrooz Fathollah, Aliha Mohammad RM, Maroofi Mahmood, Hadizadeh Vahid. Residual stresses measurement in the butt joint welded metals using FSW and TIG methods. Steel Compos Struct 2018;28(No. 6):759–66.
[29] Zhang Changqing, Wang Weijie, Jin Xin, Rong Chen, Qin Zhuo. A study on microstructure and mechanical properties of micro friction stir welded ultra-thin al-1060 sheets by the shoulder less tool. Metals 2019;9(5):507.
[30] Devireddy Krishnaja, Devuri Venkateswarlu, Cheepu Murali Mohan, Kranthi Kumar Balina. Analysis of the influence of friction stir processing on gas tungsten arc welding of 2024 auminum alloy weld zone. Int J Mech Prod Eng Res Dev 2018;8(1):243–52.
[31] Mabuwa S, Msomi V. Effect of friction stir processing on gas tungsten arc-welded and friction stir-welded 5083-H111 aluminium alloy joints. Adv Mater Sci Eng 2019:1–14.
[32] Ishak Mahadzir, Noordin Nur Fakhriah Mohd, Shah Luqman Hakim Ahmad. Feasibility study on joining dissimilar aluminum alloys aa6061 and aa7075 by tungsten inert gas (TIG). J Teknol 2015;75(7):79–84.
[33] Mohammadi-pour M, Khodabandeh A, Mohammadi-pour S, et al. Microstructure and mechanical properties of joints welded by friction-stir welding in aluminum alloy 7075-T6 plates for aerospace application. Rare Met 2016. https://doi.org/10.1007/s12598-016-0692-9.
[34] Arora A, De A, DebRoy T. Toward optimum friction stir welding tool shoulder diameter. Scripta Mater 2011;64(1):9–12.
[35] Sasaki T, Hirose Y, Sasaki K, Yasukawa S. Influence of image processing conditions of debye Scherrer ring images in x-ray stress measurement using an imaging plate. Adv X Ray Anal 1997;40:588–94.
[36] Salleh MNM, Ishak M, Shah LH, Idris SRA. The effect of ER4043 and ER5356 filler metal on welded Al 7075 by metal inert gas welding. WIT Trans Built Environ 2016;166:213–24.
[37] Smith William F, Hashemi Javad. Foundations of materials science and engineering. fourth ed. McGraw-Hill; 2006, ISBN 978-0-07-295358-9.
[38] Xu W, Liu J, Luan G, Dong C. Temperature evolution, microstructure and mechanical properties of friction stir welded thick 2219-O aluminum alloy joints. Mater Des 2009;30:1886–93.
[39] Xu W, Liu J, Luan G, Dong C. Microstructure and mechanical properties of friction stir welded joints in 2219-T6 aluminum alloy. Mater Des 2009;30:3460–7.
[40] Luijendijk T. Welding of dissimilar aluminium alloys. J Mater Process Technol 2000;103:29–35. 2000.
[41] Jia Yonggui Qin, Ou Yiwen, Wang Kehong, Liu Jizi. The influence of microstructural heterogeneity on mechanical properties of friction stir welded joints of T6-treated Al-Zn-Mg alloy 7A52Yang. Metals 2018;8(7):527.
[42] Ishak Mahadzir, Noordin Nur Fakhriah Mohd, Shah Luqman Hakim Ahmad. Feasibility study on joining dissimilar aluminum alloys aa6061 and aa7075 by tungsten inert gas (TIG). J Teknol (Sci Eng) 2015;75(7):79–84.
[43] Taira S, Tanaka K, Yamazaki T. A method of x-ray microbeam measurement of local stress and its application to fatigue crack growth problems. J Soc Mater Sci Jpn 1978;27(294):251–6.
[44] Yeni C, Sayer S, Pakdil M. Comparison of mechanical and microstructural behaviour of TIG, MIG and friction stir welded 7075 aluminium alloy. Kovove Mater 2009;47:341–7.
[45] Rossini NS, Dassisti M, Benyounis KY, Olabi AG. Methods of measuring residual stresses in components. Mater Des 2012;35:572–88.
[46] James MN. Residual stress influences in mechanical engineering. In: XVIII congreso nacional de Ingeniería Mecánica; 2010. p. 1–13.
[47] Yang YP, Babu SS, Kikel JM, Brust FW. Investigation of weld crack mitigation techniques with advanced numerical modeling and experiment-Summary. In: Lippold J, Böllinghaus T, Cross CE, editors. Hot cracking phenomena in welds III; 2011. p. 353–65.
[48] Buchanan DJ, John R. Residual stress redistribution in shot peened samples subject to mechanical loading. Mater Sci Eng A 2014;615:70–8.
[49] Zhang Zhao, Zhang Hongwu. The simulation of residual stresses in friction stir welds. J Mech Mater Struct 2007;2(5):951–64.
[50] Hwang Yeong-Maw, Kang Zong-Wei, Chiou Yuang-Cherng, Hsu Hung-Hsiou. Experimental study on temperature distributions within the workpiece during friction stir welding of aluminum alloys. Int J Mach Tool Manufact 2008;48:778–87.
[51] Yaduwanshi DK, Bag S, Pal S. Numerical modeling and experimental investigation on plasma-assisted hybrid friction stir welding of dissimilar materials. Mater Des 2016;92:166–83.
[52] Nandan R, Roy GG, Debroy T. Numerical simulation of three-dimensional heat transfer and plastic flow during friction stir welding. Metall Mater Trans 2006;37(4):1247–59.
[53] Shi L, Wu CS, Chen MA. Numerical analysis of heat transfer and material flow in reverse dual-rotation friction stir welding. In: Proceedings of the 1st international joint symposium on joining and welding, Osaka, Japan, 6–8 November; 2013.
[54] Kou S. Welding metallurgy. second ed. New York: John Willy & Sons; 2002.
[55] Mahoney MW, Rhodes CG, Flintoff JG, et al. Properties of friction-stir-welded 7075 T651 aluminum. Metall Mater Trans A 1998;29:1955–64.
[56] Mohammadzadeh Jamalian H, Farahani M, Besharati Givi MK, et al. Study on the effects of friction stir welding process parameters on the microstructure and mechanical properties of 5086-H34 aluminum welded joints. Int J Adv Manuf Technol 2016;83:611–21.
[57] Kasman Ş, Yenier Z. Analyzing dissimilar friction stir welding of AA5754/AA7075. Int J Adv Manuf Technol 2014;70:145–56.
[58] Li Yupeng, Sun Daqian, Gong Wenbiao. Effect of tool rotational speed on the microstructure and mechanical properties of Bobbin tool friction stir welded 6082-T6 aluminum alloy. Metals 2019;9(8):894.
[59] Good SH, Brown IM. Acta Mater 1979;27:1.
[60] Tszeng TC. Interfacial stresses and void nucleation in discontinuously reinforced composites. J Eng Mater Technol 2000;122:86–92.